PHYSICAL REVIEW B **112**, 115145 (2025)

Pressure-tuned magnetism and band-gap modulation in layered Fe-doped $CrCl_3$

Mahmoud Abdel-Hafiez,[1,2,3,4,*] Govindaraj Lingannan,[3] Aya Ali,[1] Lukas Gries,[5] R. Thiyagarajan,[6,7] Md Ezaz Hasan Khan,[3]
Anas Abutaha,[8] T. A. Abdel-Baset,[4,9] Kei Uemura,[10] Masaki Mito,[10] Vladislav Borisov,[11,12] Anna Delin,[13,14,15]
Rüdiger Klingeler,[5] M. S. Ramachandra Rao,[6,7] and Olle Eriksson[11,12]

[1]*Center for Advanced Materials Research, Research Institute of Sciences and Engineering, University of Sharjah,*
Sharjah 27272, United Arab Emirates
[2]*Department of Applied Physics and Astronomy, University of Sharjah, P. O. Box 27272 Sharjah, United Arab Emirates*
[3]*University of Doha for Science and Technology, Doha, Qatar*
[4]*Department of Physics, Faculty of Science, Fayoum University, Fayoum, 63514, Egypt*
[5]*Kirchhoff Institute of Physics, Heidelberg University, INF 227, D-69120 Heidelberg, Germany*
[6]*Quantum Centre of Excellence for Diamond and Emergent Materials (QuCenDiEM), Indian Institute of Technology Madras,*
Chennai 600036, India
[7]*Department of Physics, Indian Institute of Technology Madras, Chennai 600036, India*
[8]*Qatar Environment and Energy Research Institute (QEERI), Hamad Bin Khalifa University, Doha 34110, Qatar*
[9]*Department of Physics, Faculty of Science, Taibah University, Yanbu, 46423, Saudi Arabia*
[10]*Graduate School of Engineering, Kyushu Institute of Technology, Fukuoka 804–8550, Japan*
[11]*Department of Physics and Astronomy, Uppsala University, Uppsala, 751 20, Sweden*
[12]*Wallenberg Initiative Materials Science for Sustainability (WISE), Uppsala University, Uppsala, 751 20, Sweden*
[13]*Department of Applied Physics, KTH Royal Institute of Technology, 516, SE-75121, Stockholm, Sweden*
[14]*Swedish e-Science Research Center (SeRC), KTH Royal Institute of Technology, SE-10044 Stockholm, Sweden*
[15]*Wallenberg Initiative Materials Science for Sustainability (WISE), KTH Royal Institute of Technology, SE-10044 Stockholm, Sweden*

(Received 13 February 2025; revised 30 July 2025; accepted 2 September 2025; published 25 September 2025)

We report a comprehensive investigation of the structural, magnetic, vibrational, and optical properties of Fe-doped $CrCl_3$ under varying external pressures. By integrating high-pressure experimental techniques, including Raman spectroscopy, photoluminescence (PL), magnetization, and thermal expansion measurements, with density functional theory (DFT) calculations, we uncover pressure-driven phase and magnetic transitions in this layered van der Waals material. At ambient pressure, Raman spectra exhibit all six expected Raman-active modes, which systematically blueshift with increasing pressure. A distinct change occurs in A_g^3 mode near 9.2 GPa, suggesting an isostructural phase transition (IST), similar to that observed in pristine $CrCl_3$ around 11 GPa. PL measurements indicate a band gap of 1.48 eV at approximately 0.6 GPa, which increases with pressure up to 9.2 GPa, followed by a slight decrease beyond this point. This further confirms the occurrence of the IST. Magnetization measurements at ambient pressure under 0.001 T magnetic field reveal two magnetic transitions: T_N at 14.3 K and T_C at 16 K, indicating the coexistence of antiferromagnetic (AFM) and ferromagnetic (FM) phases. Upon applying pressure, T_N and T_C gradually become suppressed, and T_N disappears by 2 GPa. The transition width associated with T_C broadens beyond 0.5 GPa, highlighting the pressure-enhanced FM behavior. Field-dependent magnetization at ambient pressure shows complete suppression of T_N above 0.4 T, with FM ordering dominating at higher fields. At 1.2 GPa, both T_N and T_C shift to lower temperatures. Notably, T_N is suppressed above 0.2 T and only FM order remains. Grüneisen analysis of the uniaxial thermal expansion confirms the competition between FM and AFM interactions and yields very large uniaxial pressure effects of $-143\%/\mathrm{GPa}$ and $+43\%/\mathrm{GPa}$, at TN and TC, respectively. DFT calculations for pure $CrCl_3$ are consistent with experimental data and predict a pressure-induced suppression of interlayer AFM exchange, accompanied by the stabilization of FM intralayer coupling through enhanced Cr–Cl–Cr superexchange pathways. These calculations suggest an AFM-to-FM interlayer stacking transition occurring near 1 GPa. Furthermore, increasing Fe doping appears to support the persistence of AFM character. Our findings establish Fe-doped $CrCl_3$ as a promising platform for pressure-tunable magnetism. The ability to manipulate FM and AFM interactions through external pressure and magnetic fields opens avenues for applications in sensors, spintronic devices, and other functional two-dimensional magnetic systems.

DOI: 10.1103/v7l7-f3wj

I. INTRODUCTION

Significant advancements in two-dimensional (2D) materials research were catalyzed by the ground-breaking isolation of monolayer graphene from graphite in 2004 [1]. This

---

[*] Contact author: mahmoudhafiez@gmail.com

2469-9950/2025/112(11)/115145(12)

milestone work expanded the horizons of condensed matter physics, leading to the discovery of diverse and novel properties in a wide range of 2D quantum materials. Among these, van der Waals (vdW) materials have garnered particular interest due to their unique magnetic, electrical, and optoelectronic properties, making them highly promising for next-generation technologies [2,3]. These materials are defined by weak interlayer van der Waals forces and strong intralayer covalent bonding, giving rise to remarkable magnetic behaviors with significant anisotropy [4,5]. Furthermore, the investigation of spin dynamics and the establishment of long-range ferromagnetic (FM) order in 2D vdW systems underline their substantial potential for spintronic applications, where control over spin degrees of freedom can revolutionize information processing and storage technologies [6,7]. An important class of vdW 2D materials is the family of transition-metal trihalides (TMTHs) which have the general formula MX_3, where M represents a transition-metal cation and X is a halogen anion. The long-range magnetic order is stabilized in TMTHs by magnetic anisotropy that rises from spin-orbit coupling and crystal field effects. This unique combination of electronic and magnetic features positions TMTHs as ideal candidates for advancing fundamental research and practical applications in spintronics and quantum information science [8,9].

Chromium-based halide magnets, specifically CrX_3 ($X =$ Cl, Br, I), is one of the important TMTH materials with highly tunable magnetic properties. As the halogen's size is increased from Cl to I, the FM transition appears at 14 K (for $CrCl_3$) [10,11], 34 K (for $CrBr_3$) [12,13], and 61 K (for CrI_3) [14,15], i.e., larger halogens contribute the strong spin-orbit coupling, significantly to the magnetocrystalline anisotropy by direct and indirect exchange interactions. According to the Goodenough-Kanamori-Anderson (GKA) rules, the Cr–X–Cr bond angle determines the type of superexchange interaction [16–18] and that Cr-Cr magnetic pair interactions change sign from antiferromagnetic (AFM) to FM as the Cr-Cr distance is altered [19].

These properties of vdW-layered 2D materials could be modified further by external high pressure (HP), which is an effective and impurity-free tool. It allows precise modulation of lattice uniformly, thereby altering interlayer and intralayer bonding interactions of vdW systems subsequently all other physical properties without introducing chemical impurities [20,21], for example, increase of pressure shifts T_C of CrI_3 from 61 to 66 K under 3 GPa, and it is reduced to 10 K at 21 GPa. Theoretical calculations suggest that the room-temperature analog of this phenomenon corresponds to a semiconductor-to-metal transition at 21 GPa. This pressure-induced metallization is further confirmed by HP Raman measurements but at slightly earlier pressure of 17 GPa [22]. In the case of $CrBr_3$, T_C decreases under pressure and FM behavior is completely suppressed around 8 GPa. HP Raman measurements on this system revealed an anomaly at 15 GPa which potentially related to metallization property [23–25]. $CrCl_3$ exhibits short-range FM order at 17 K and long-range AFM order at 14 K [11,26]. The disappearance of the A_g Raman mode of $CrCl_3$ was observed at 11 GPa [10,27].

The internal doping will easily modify the properties of these systems such as the following: Doping CrI_3 with small amounts of Mn or V shifts T_C to lower temperatures [28,29]. Mn-doped CrI_3 shows higher saturation magnetization, while V-doped CrI_3 exhibits higher coercivity and increased magnetocrystalline anisotropy [29]. The doping of alkali metals in $CrCl_3$ increases T_C from 23 to 66 K, which is attributed to the electron transfer by boosting the magnetic ordering [30]. Magnetic coupling parameters are decreased by doping, and linear Dirac dispersion originates from the honeycomb lattice formed by Cr atoms. Theoretical predictions suggests that the suitable doping will bring direct and narrow band gaps to the chromium-based halide magnets [31].

Among these three chromium-based halide magnets, $CrCl_3$ has in-plane magnetic anisotropy and A-type AFM behavior [8,31]. Pristine $CrCl_3$ is a wide-gap semiconductor; while doping it shifts the Fermi level and induces a transition to a half-metallic state [30]. In this study we systematically investigate the effects of chemical doping by Fe at the Cr site in $CrCl_3$, i.e., $Cr_{1-x}Fe_xCl_3$ ($x = 0$, 0.01, 0.02, 0.03, 0.04, and 0.05), as well as the influence of HP on the highly doped composition $Cr_{0.95}Fe_{0.05}Cl_3$. The goal is to elucidate the impact of both internal (chemical) and external (physical) perturbations on the structural, vibrational, and magnetic properties of the system. To this end, we employ a combination of experimental techniques, including Raman spectroscopy, photoluminescence (PL), dilatometry, and magnetization measurements under varying temperature, magnetic field, and pressure conditions. Fe is selected as the dopant due to its well-known FM characteristics, which contrast with the AFM nature of Cr, potentially enhancing FM ordering in the system. Furthermore, the larger atomic radius and higher atomic number of Fe compared to Cr can mimic the effect of chemical pressure by expanding the unit-cell volume. The experimental results are supported by first-principles calculations based on density functional theory (DFT).

II. EXPERIMENTAL AND COMPUTATIONAL DETAILS

Chromium trichloride ($CrCl_3$) was synthesized using the chemical vapor transport (CVT) method. High-purity $CrCl_3$ powder is sealed in an evacuated quartz ampoule along with a transport agent, iodine, which facilitates the sublimation and recrystallization of $CrCl_3$ in a temperature gradient. The ampoule is placed in a two-zone furnace, where the source zone is maintained at a higher temperature (650 °C–700 °C) and the growth zone at a lower temperature (550 °C–600 °C) [32]. Over several days to weeks, $CrCl_3$ vapor gradually deposits in the cooler zone, forming well-defined layered single crystals. To introduce iron (Fe) into the $CrCl_3$ lattice, a controlled amount of $FeCl_3$ and additional Fe precursors are added to the $CrCl_3$ starting material, ensuring a stoichiometric composition corresponding to $Cr_{1-x}Fe_xCl_3$ with Fe concentrations $x =$ 0.01, 0.02, 0.03, 0.04, and 0.05. The mixture is then sealed in an evacuated quartz ampoule with iodine as the transport agent and subjected to the same CVT growth conditions as pure $CrCl_3$.

Room-temperature (x-ray diffraction) XRD measurements were carried out using a Rigaku SmartLab diffractometer with a Cu $K\alpha$ x-ray source. Ambient and HP Raman-scattering measurements were performed using a Renishaw micro-Raman spectrometer. A 532-nm (2.33 eV) diode laser was employed as the excitation source, enabling a diffraction-limited laser spot with a diameter of ∼1.0 µm and a spectral resolution of around 1 cm^{-1}. *In situ*, HP Raman, and PL spectra were obtained using a symmetric diamond anvil cell (DAC) with diamond anvils of 500-µm culet size. A 300-µm-thick SS301 stainless steel gasket was preindented to a thickness of 100 µm to enhance its hardness, and a 200-µm-diameter hole was drilled in the center of the gasket to create the sample chamber. Silicon oil was used as the pressure-transmitting medium. The pressure inside the sample chamber was measured using the ruby fluorescence method, using ∼5-µm ruby chips placed with the sample for calibration. During HP measurements, a waiting period of at least 30 min was allowed between each pressure increment to ensure that pressure equilibria were reached. The Raman spectra were fitted with Lorentzian profiles to extract mode frequencies and peak widths.

The ambient dc magnetization measurements were performed in a Magnetic Properties Measurement System (MPMS3) on $\mathrm{Cr_{0.95}Fe_{0.05}Cl_3}$ in the temperature range of 2–300 K and in fields up to 7 T applied along the crystallographic *c* direction. HP ac magnetization measurements have been carried out in the above said system using a miniature DAC with a culet size of diamond anvils of 800 µm. The sample hole with a diameter of 300 or 400 µm was prepared in a BeCu gasket with initial thickness of 300 µm. Several pieces of crystals and liquidlike pressure-transmitting medium Apiezon J oil (M & I Materials Limited) were held in the sample cavity with some ruby balls. The pressure at room temperature was evaluated by measuring the fluorescence of ruby balls inside the sample chamber. The increase in pressure at liquid helium temperature against that at room temperature is at most 10%.

High-resolution dilatometry measurements were performed in a three-terminal capacitance dilatometer from Küchler Innovative Measurement Technologies [33,34]. The measurements were done in a home-built setup in a variable-temperature insert (VTI) of an Oxford Instruments magnet system at zero field and B = 15 T applied along the direction of measured length changes [35]. The sample thickness in the measurement direction, i.e., the crystallographic *c* axis, was 0.149 mm. The linear thermal expansion coefficients $\alpha_c = 1/L_c(300\,\mathrm{K}) \times \partial L_c(T)/\partial T$ are derived from the relative length changes. To explore HP properties of $\mathrm{CrCl_3}$ from first principles, we used DFT with static mean-field correlation available in the vasp code [36]. The exchange-correlation energy was described using the PBE-parametrized generalized-gradient approximation. The rotationally invariant Lichtenstein formulation of GGA+*U*, with $U = 3$ eV and $J_H = 0.6$ eV, was used for a more accurate description of electronic correlations, needed for correctly capturing the insulating character of $\mathrm{CrCl_3}$. The chosen values of *U* and J_H parameters provide a reasonable value of the electronic band gap and the Cr magnetic moment magnitude and are kept fixed for all studied pressures.

III. RESULTS

A. XRD characterization

Figures 1(a) and 1(b) represent the room-temperature XRD patterns of $\mathrm{Cr_{1-x}Fe_xCl_3}$ ($x = 0.01$ and 0.05), respectively. Rietveld refinement has been carried out on these XRD profiles using the GSAS-II package, and it confirms that both compositions crystallize in a monoclinic structure with space group of $C2/m$. The refined lattice parameters of the $\mathrm{Cr_{0.99}Fe_{0.01}Cl_3}$ sample are $a = 5.959(2)$ Å, $b = 10.146(9)$ Å, $c = 6.035(9)$ Å, with a monoclinic angle $\beta = 109.02°$, and a unit-cell volume of 345.1 Å^3. In comparison, the $\mathrm{Cr_{0.95}Fe_{0.05}Cl_3}$ sample exhibits expanded lattice parameters of $a = 6.390(2)$ Å, $b = 10.893(1)$ Å, and $c = 6.359(9)$ Å, with $\beta = 107.39°$ and a unit-cell volume of 422.4 Å^3 [10,27]. The systematic increase in lattice parameters and unit-cell volume with increasing bigger Fe content at the place of Cr suggests successful substitution of Fe into the $\mathrm{CrCl_3}$ lattice. We did not observe any impurity peaks in our samples. To confirm the compositional ratio further, EDX has been carried out on these samples and the results are shown in Supplemental Material, Fig. S1 [37]. The results confirm that the actual compositions are consistent with the intended stoichiometries within experimental uncertainty. It is worth noting that our samples exhibit an unexpectedly large expansion in unit-cell volume with increasing Fe doping. To gain a deeper understanding of this observation, we intend to carry out further structural investigations using high-resolution transmission electron microscopy (TEM) and synchrotron XRD.

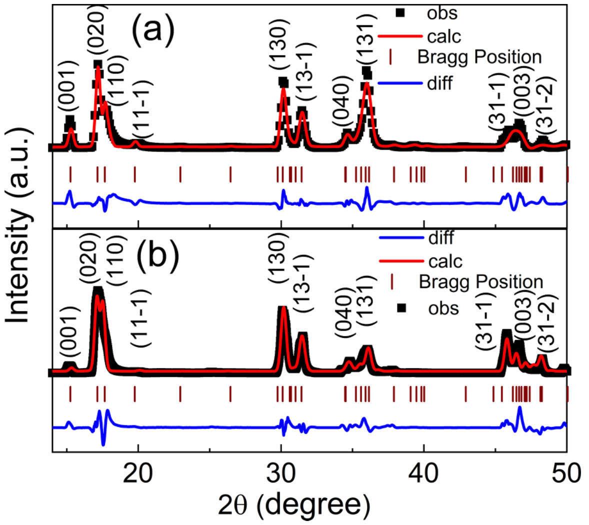

FIG. 1. (a) Measured x-ray diffraction pattern of $\mathrm{Cr_{1-x}Fe_xCl_3}$ with (a) $x = 0.01$ and (b) $x = 0.05$ at ambient pressure and room temperature, together with the Rietveld refinement results (solid red lines).

B. Raman measurements

Figure 2 displays the Raman spectra of $\mathrm{Cr_{1-x}Fe_xCl_3}$ samples with varying Fe content ($x = 0.01$, 0.02, 0.03, 0.04, and 0.05), and the estimated Raman peak positions and FWHM of the corresponding Fe-doped samples are summarized in Table I.

These peaks are translational motion (*T'*) of Cl and Cr atoms of the $\mathrm{CrCl_3}$ structure and are attributed to Raman intralayer vibrational modes of A_g only, since the prepared sample is a flakey, thin-layer system. These are assigned as A_g^1, A_g^2, A_g^3, A_g^4, A_g^5, and A_g^6, respectively, as shown in Fig. 2

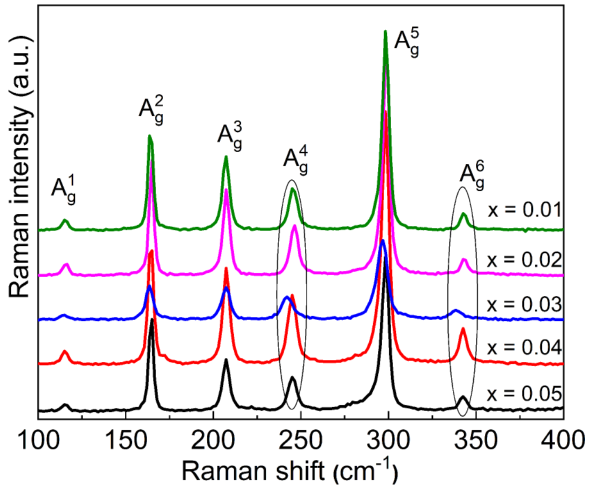

FIG. 2. Measured Raman spectra of $Cr_{1-x}Fe_xCl_3$ ($x = 0.01$, 0.02, 0.03, 0.04, and 0.05) samples under ambient conditions using a 532-nm laser source.

[38,39]. Upon doping of Fe with $CrCl_3$, the Raman profile slightly shifts to lower wave numbers (i.e., redshift) and become softened as well. Here, the interlayer spacing of $CrCl_3$ lattice expands due to bigger atomic size of Fe at Cr places and so forces constants of Cr–Cl and Cl–Cl bonding to weaken due to this distortion. Consequently, the vibrational frequencies of Raman peaks also decreased. These results are confirmed by XRD data.

C. Pressure-dependent Raman study

HP Raman spectroscopy was employed to investigate the vibrational transitions in $Cr_{0.95}Fe_{0.05}Cl_3$, the sample with the highest doping Fe concentration in this series. Measurements were conducted up to approximately 16 GPa of hydrostatic pressure, and the evolution of phonon modes was explored under compression and is shown in Fig. 3(a). At the initial pressure 0.52 GPa, $Cr_{0.95}Fe_{0.05}Cl_3$ exhibits six peaks at 114.2, 163.6, 207.1, 244.8, 298.3, and 342.3 cm^{-1} with these already assigned Raman-active modes of A_g^1, A_g^2, A_g^3, A_g^4, A_g^5, and A_g^6. As pressure increases, all the modes exhibit a smooth shift toward higher frequencies (blueshift) with broadening, except for A_g^3.

TABLE I. Measured Raman modes of vibrations for $Cr_{1-x}Fe_xCl_3$ ($x = 0.01$, 0.02, 0.03, 0.04, and 0.05).

	Raman shift (cm−1)						
x	A_g^1	A_g^2	A_g^3	A_g^4	A_g^5	A_g^6	References
0 (DFT)	118	166	207	250	300	345	[38,39]
0 (Exp)	116.5	165.3	208.6	246.5	300.0	344.5	[27]
0.01	115.3	164.2	207.1	245.6	298.3	343.0	This work
0.02	115.7	164.7	207.4	246.2	298.5	343.2	
0.03	114.7	163.5	207.1	242.2	296.3	338.7	
0.04	115.2	164.3	207.4	245.0	298.1	342.6	
0.05	115.3	164.5	207.2	245.1	298.1	342.5	

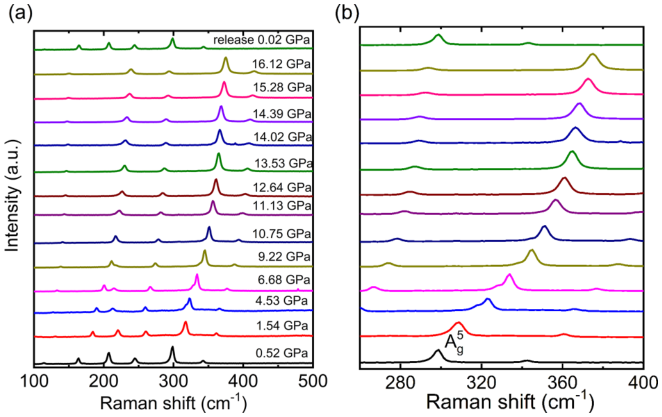

FIG. 3. (a) Measured Raman spectra for $Cr_{0.95}Fe_{0.05}Cl_3$ at selected pressures at room temperature, and (b) enlarged view of A_g^5 mode.

Figure 3(b) shows the enlarged view of Fig. 3(a) around A_g^5 which illustrates two distinct rates of change in blueshift of the Raman profile at 9.23 GPa. It suggests a possible isostructural phase transition (IST). Upon decompression, the Raman profile exhibits the redshift and reappears at 0.02 GPa, which confirms that the structural transition is reversible. This reversible nature of the Raman peaks highlights the robustness and stability of the $Cr_{0.95}Fe_{0.05}Cl_3$ lattice under HP conditions.

For a detailed analysis of the pressure effect on Raman spectra of $Cr_{0.95}Fe_{0.05}Cl_3$, the Raman peak positions and FWHMs at different pressures were estimated through Lorentzian fitting and shown in Figs. 4(a)(i-vi) and 4(b)(i-vi), respectively. The peaks against pressure follow two distinct rates with the appreciable change in slope at 9.23 GPa which suggests a possible IST. The linear fitting on each peak of Fig. 4(a)(i-vi) in two different pressure regimes brought the values of higher rates of 2.82, 5.39, 1.18, 3.36, 5.31, 5.15 cm^{-1}/GPa till 9.23 GPa and lower rates of 1.76, 3.34, 2.94, 4.52, 4.18 cm^{-1}/GPa above 9.23 GPa. The difference in rates of blueshifts of each peak before and after 9.23 GPa is accompanied with the pronounced broadening of the corresponding peaks as shown in Fig. 4(b)(i-vi). In particular, the A_g^3 mode disappeared and/or merged with A_g^2 at the critical pressure of 9.23 GPa.

This phenomenon is directly evident for the presence of IST in the $Cr_{0.95}Fe_{0.05}Cl_3$ system. For reference, this same phenomenon of IST has been already reported in pure $CrCl_3$, CrI_3, and $CrBr_3$ systems at 11 GPa, 7.2 GPa, and 9.5 GPa [10,22,24].

D. Pressure-dependent photoluminescence

Figure 5(a) shows the HP PL spectra of $Cr_{0.95}Fe_{0.05}Cl_3$, while Fig. 5(b) illustrates the evolution of the optical energy gap as a function of pressure up to 14.41 GPa. The PL spectrum at 0.65 GPa reveals an optical energy gap of 1.48 eV, which closely corresponds to its indirect band gap of parent $CrCl_3$ (1.67 eV) [10]. As the pressure increases, the PL peak shifts toward shorter wavelengths until ∼9 GPa. By further increasing pressure, PL peaks shift to higher wavelengths

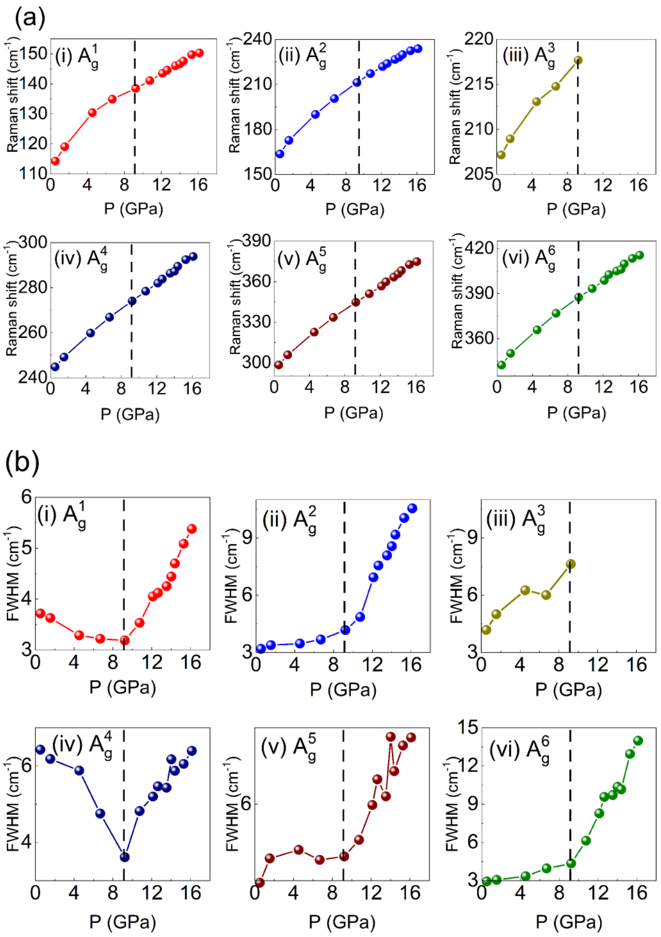

FIG. 4. (a) Raman shift peak positions as a function of pressure (six panels for each peak), and (b) FWHM of Raman peaks as a function of pressure (six panels for each peak) of $Cr_{0.95}Fe_{0.05}Cl_3$. Dashed lines are guides to the eye for the change in the slopes at pressure 9.23 GPa.

very slightly up to 14.4 GPa. The estimated energy gaps (E_g) against pressure points are shown in Fig. 5(b), indicating the presence of a pressure-induced increase in the energy band gap until 9 GPa with a trend change of very little decreasing of E_g above 9 GPa, which may be attributed to the onset of an IST [16]. Pressure-induced IST has been reported in parent $CrCl_3$ systems at ∼11 GPa through HP XRD measurements. Here pressure shortens the metal Cr–ligand Cl bonds slightly without altering the space group of the system, resulting in an upward shift of the conduction band or a downward shift of the valence band, thereby widening the band gap. In our Fe-doped $CrCl_3$ system, IST has been observed slightly early at a pressure of 9 GPa as the metallic nature of doped Fe supports the band-gap reduction easily under the high-pressure regime.

This phenomenon is accompanied by a magnetic phase transition from FM to AFM in parent $CrCl_3$. However, in the synthesized $Cr_{0.95}Fe_{0.05}Cl_3$, a similar energy-band-gap trend changes and the presence of IST is observed at ∼9 GPa by HP Raman and HP PL measurement. So, these results confirm that the switching magnetic behavior under pressure is possible in our doped sample [10]. Upon decompression, the system returns to its original phase, with the energy gap recovering to 1.48 eV at 0.59 GPa. This reversibility indicates that the structural and electronic changes induced by pressure are not permanent, highlighting the resilience of the $CrCl_3$ lattice.

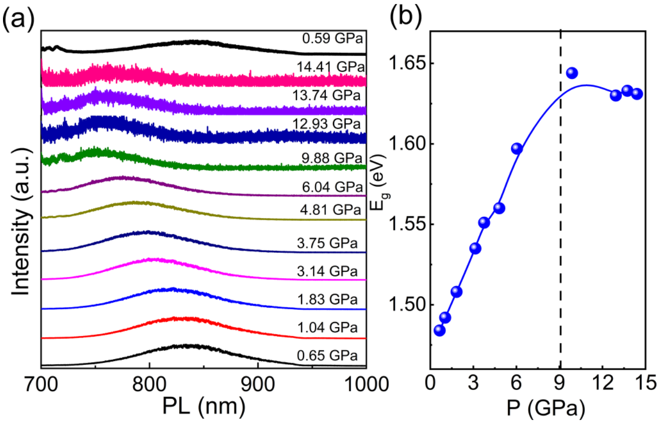

FIG. 5. (a) Measured PL spectra of $Cr_{0.95}Fe_{0.05}Cl_3$ at selected pressures at room temperature, and (b) calculated energy band gap as a function of pressure from the PL study.

E. Pressure-dependent magnetization

Figure 6 shows the measured magnetization data of $Cr_{0.6}Fe_{0.4}Cl_3$ as a function of temperature at $B = 10$ mT and $B = 1$ T applied along the crystallographic c axis. The FM nature of $Cr_{0.6}Fe_{0.4}Cl_3$ studied at hand is illustrated by a sharp increase of magnetization, at low temperatures, while long-range AFM order is signaled by a peak in M (T, $B =$ 10 mT) at the Néel temperature (T_N) = 13.5 K. The saturation magnetization (data not shown), at $T = 1.8$ K, assumes $M_{sat} =$ 2.88(3) μ_B/f.u., which agrees with the 2.9 μ_B/f.u. reported in Ref. [26] but is slightly smaller than 3.0 μ_B/f.u. from Ref. [11]. In addition, Fisher's specific heat reveals a distinct anomaly

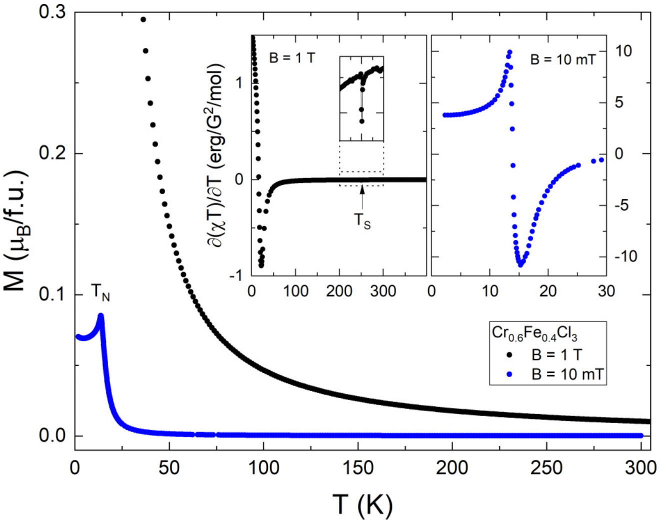

FIG. 6. Temperature dependence of the magnetization measured on $Cr_{0.6}Fe_{0.4}Cl_3$ at $B = 10$ mT and $B = 1$ T applied along the crystallographic c axis. Left inset: Fisher's specific heat $\partial(\chi T)/\partial T$ with an enlargement of the anomaly at the structural transition at $TS = 251$ K at $B = 1$ T. Right inset: Fisher's specific heat at $B = 10$ mT.

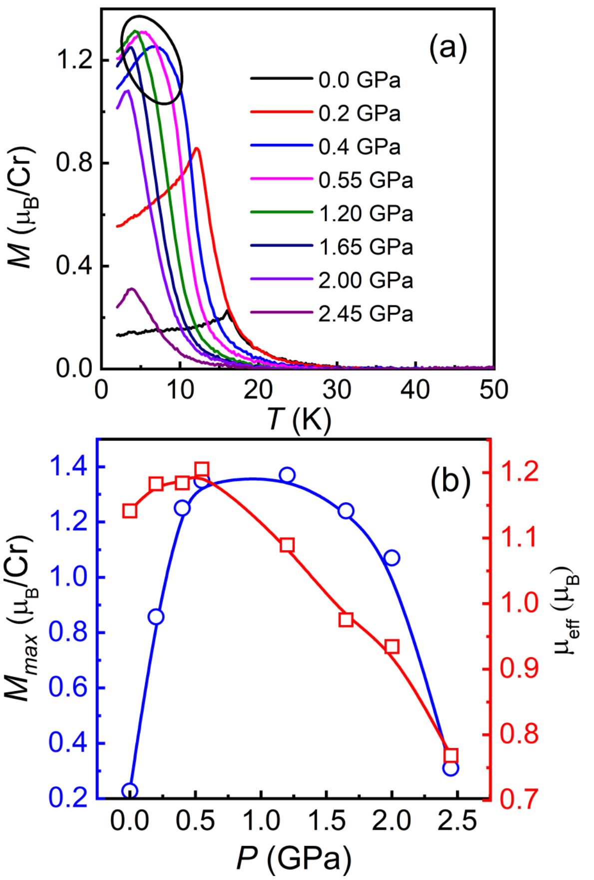

FIG. 7. (a) Measured temperature-dependent ac magnetization data of $Cr_{0.95}Fe_{0.05}Cl_3$ under various fixed pressures up to 2.5 GPa in the warming process after field cooling from 50 K down to 2 K under the magnetic field of 0.001 T. (b) Pressure dependence of the maximum magnetic moment (M_{max}) at the transition temperature (blue open circle symbols) in the left axis and the effective paramagnetic moment (μ_{eff}) (red open square symbols) in the right axis.

at $T_S = 251(1)$ K associated with the IST reported previously [11].

Figure 7(a) presents the temperature-dependent ac magnetization [$M(T)$] data of $Cr_{0.95}Fe_{0.05}Cl_3$ under various fixed pressures up to 2.5 GPa, measured at an applied dc magnetic field of 0.001 T. At 0 GPa, the sample exhibits T_C of 16 K and the T_N of 14.3 K. Upon increasing pressure, the $M(T)$ curve shifts toward the lower-temperature side, and the magnetic moment increases sharply up to 0.4 GPa. Beyond this point, the rate of increase diminishes, peaking at around 1.2 GPa, and then shows a pronounced decline above 1.65 GPa. Simultaneously, the sharp cusp associated with the AFM transition become progressively broader under pressures of 0.4, 0.55, and 1.2 GPa. This broadening suggests a suppression of AFM order and an enhancement of FM behavior, as indicated by the black circle in the figure.

The rate of decrease in T_C and T_N is particularly high in the low-pressure regions, i.e., below 0.5 GPa. The observed suppression of both T_C and T_N with increasing pressure indicates that pressure weakens the Cr–Cr and Cr–Cl magnetic exchange interactions by modifying the interlayer and intralayer distances as well as the bond angles [10,21–23]. Additionally, we analyzed the maximum magnetic moment (M_{max}) at the transition temperature (T_C) and the effective paramagnetic moment (μ_{eff}) for each pressure, as shown in Fig. 7(b) (blue open box and red open circles, respectively). From these plots, it is evident that M_{max} increases up to 1.2 GPa. Meanwhile, T_N decreases monotonically across the entire pressure range. The consistently positive Weiss temperatures indicate that intraplanar ferromagnetic interactions dominate the magnetic response, and these interactions become more prominent above 0.5 GPa, leading to a broadening of the ferromagnetic transition [11].

The increase in magnetic moment up to 1.2 GPa suggests enhanced intralayer coupling and a reduction in interlayer exchange interactions, favoring a more ferromagneticlike magnetic state [22]. The monotonic decrease in T_C and T_N with increasing pressure is attributed to pressure-induced modifications in the Cr–Cr distances and Cr–Cl–Cr bond angles. The initial enhancement in magnetization at low pressures is indicative of AFM-like behavior, which gradually evolves toward FM ordering with further pressure increase (see the Supplemental Material, Figs. S2–S6 [37]). This trend is further supported by the behavior of the effective paramagnetic moment (μ_{eff}), which rises up to 0.55 GPa and then decreases with pressure up to 2.45 GPa. Notably, the μ_{eff} values remain significantly lower than the expected spin-only value for Cr^{3+} ions (3.87 μ_B), highlighting the complex magnetic interactions in the $CrCl_3$ system.

To further explore the influence of magnetic fields under pressure, $M(T)$ measurements were carried out at 0 and 1.2 GPa under applied magnetic fields ranging from 0.001 to 1 T, as shown in Fig. 8. At 0 GPa under 0.001 T applied magnetic field, both FM and AFM are observed at 16 and 14.3 K [Fig. 8(a)] (see the Supplemental Material, Fig. S7 [37]). As the magnetic field increases, T_N shifts to lower temperatures and is completely suppressed above 0.4 T. This behavior is consistent with that observed in parent $CrCl_3$ [11]. Above 0.4 T, ferromagnetic behavior is enhanced by the applied field, with T_C increasing to 22 K at 1 T (see the Supplemental Material, Figs. S8–S10 [37]). In this regime, magnetic moments are aligned ferromagnetically within the layers, and although the layers are antiferromagnetically stacked, the external magnetic field aligns all magnetic moments parallel to its direction, resulting in a net ferromagneticlike response [11]. Figure 8(b) presents the $M(T)$ behavior at a pressure of 1.2 GPa. Under an applied field of 0.001 T, both T_N and T_C shift to lower temperatures, appearing at 4.6 and 6.8 K, respectively. With increasing magnetic field, T_N is fully suppressed above 0.2 T while T_C increases, reaching 10 K at 0.4 T. At higher fields, particularly above 0.1 T, ferromagnetic characteristics become increasingly prominent at both 0 GPa and 1.2 GPa, likely due to the alignment of crystallites along the direction of the applied field (see the Supplemental Material, Figs. S11–S14 [37]).

F. Uniaxial pressure effects: Thermal expansion and Grüneisen scaling

Our studies of the thermal expansion along the c axis provide further information on the magnetoelastic coupling

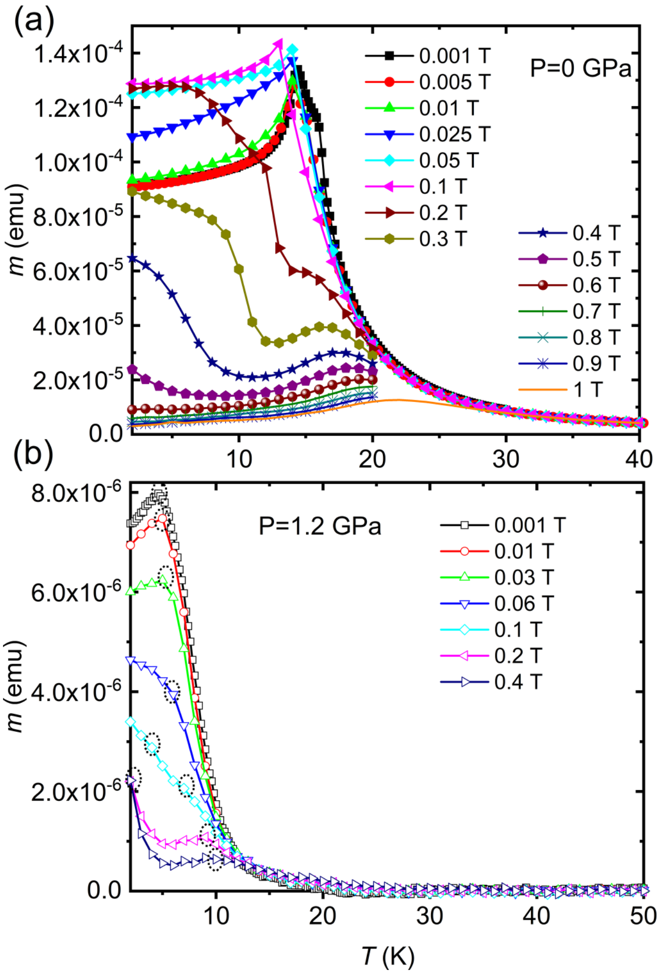

FIG. 8. Temperature dependence of ac magnetization of $Cr_{0.95}Fe_{0.05}Cl_3$ under a fixed pressure of 0 GPa (a) and 1.2 GPa (b): (a) applied magnetic fields ranging from 0.001 T to 1 T, and (b) applied magnetic fields from 0.001 T to 0.4 T.

in $CrCl_3$ and on the uniaxial pressure dependence of T_N. As it is displayed in Fig. 9(a), the c axis expands quasilinearly upon heating above ∼80 K. At high temperature, this changes only marginally when applying a high magnetic field of 15 T. Upon cooling, anomalies in the vicinity of T_N and clear effects of the magnetic field on the relative length changes signal significant magnetoelastic coupling. This is particularly evident if the thermal expansion coefficient α_c is considered [Fig. 9(b)]. Specifically, upon cooling it displays a jumplike decrease at T_N and a change in slope at T_C.

When applying $B = 15$ T, the jump at T_N vanishes and α_c decreases in the vicinity of T_C, i.e., up to about 30 K, but increases at higher temperatures. It is straightforward to attribute this behavior to field-induced suppression of the antiferromagnetically ordered phase [11] and the increase of ferromagnetic correlations above T_N, i.e., shift of associated ferromagnetic entropy to higher temperatures. This behavior in particular shows that short-range ferromagnetic correlations are associated with an increase in α_c. Hence, according to the Grüneisen relation $\partial \ln(\epsilon)/\partial p_i = V_m \alpha_i / c_p$, our data imply the positive uniaxial pressure dependence of the energy

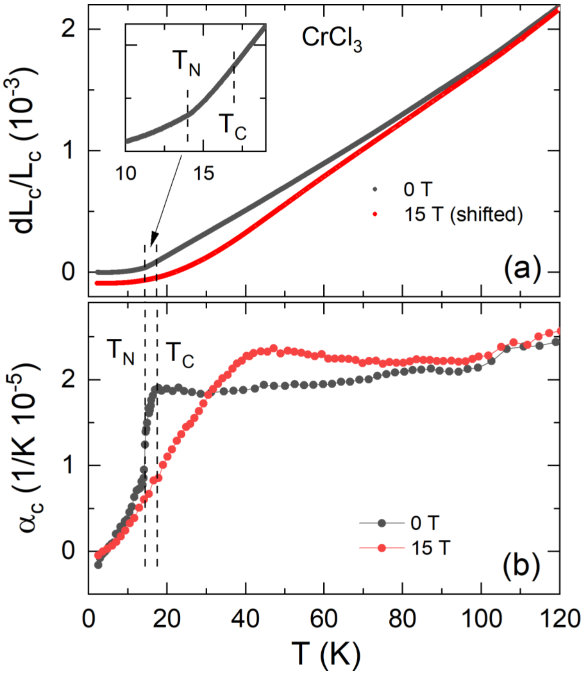

FIG. 9. (a) Uniaxial length changes and (b) thermal expansion coefficient α_c of $CrCl_3$. Vertical dashed lines are a guide to the eye. Data at 15 T have been shifted by -7×10^{-5} to match the zero field data at 120 K and to illustrate the field effect.

scale ϵ_1 driving in-plane ferromagnetic correlations [40,41]. In contrast, the jumplike decrease in α_c, at T_N, unequivocally demonstrates that $\partial\epsilon_2/\partial p_c < 0$, with ϵ_2 being the driving energy of long-range AFM order. These results strongly support the magnetization measurement results at ambient pressure.

This is further illustrated in Fig. 10 where α_c is compared to recently reported specific heat data [11]. The jump in α_c at T_N corresponds to the sharp anomaly in c_p. In addition, the regime of particularly pronounced anomalous entropy changes between T_N and T_C corresponds to a regime of decreasing α_c. The comparison of c_p and α_c is illustrated by the overall Grüneisen ratio $\gamma_c = \alpha_c/c_p$ in Fig. 10(c).

The magnetic Grüneisen ratio which in principle can be obtained by subtracting the phonon contributions to c_p and α_c cannot be derived reliably in the case at hand. As illustrated in Fig. 10(a), we interpret the reported magnetic specific heat in Ref. [11] (not shown here) as only a very small portion of the total heat capacity, which in the temperature regime under study is by far dominated by magnetic degrees of freedom. The background estimated in Ref. [42], as well as our own studies on isostructural materials, implies that the specific heat, at T_N, is by far ($\gg 90\%$) dominated by magnetic entropy changes. This analogously holds for the thermal expansion where the phonon background can be estimated from c_p^{bgr} by means of phononic Grüneisen scaling. The total Grüneisen scaling hence provides meaningful information on magnetic degrees of freedom in $CrCl_3$.

As seen in Fig. 10, our data imply three distinct temperature regimes: (1) Above T_C, γ_c increases upon cooling and assumes a broad maximum around T_C. (2) At $T_N \leqslant T \leqslant T_C$,

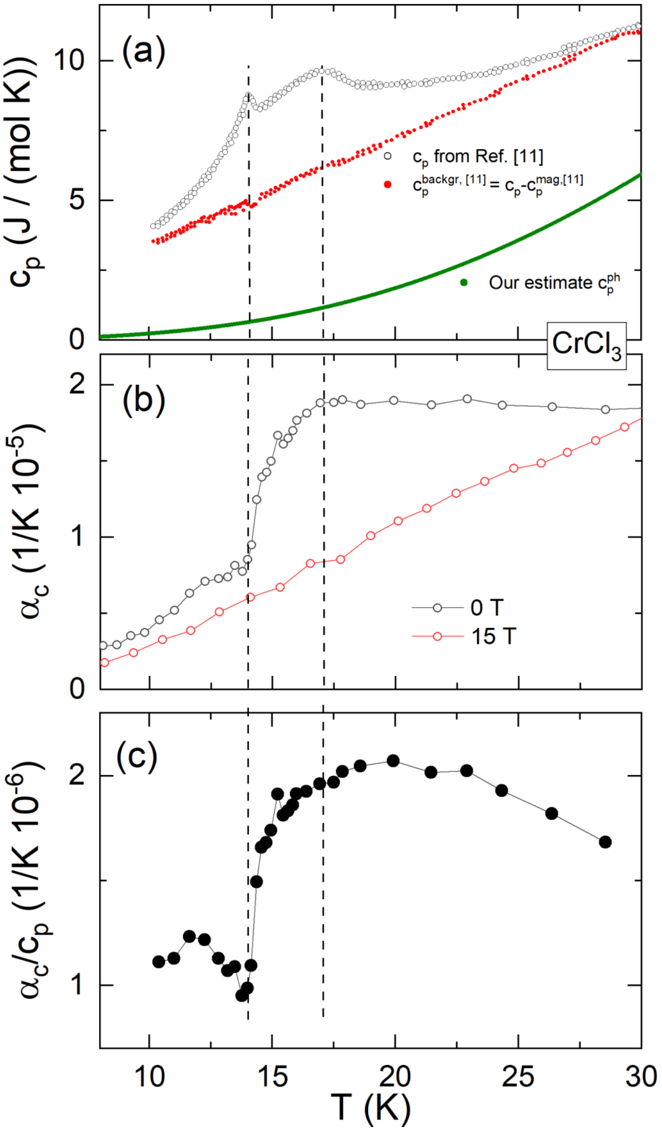

FIG. 10. (a) Specific heat C_P from Ref. [11] and (b) thermal expansion coefficient α_c of CrCl$_3$. (c) Grüneisen ratio c_p/α_c. In (a), we calculated the background used in [11] from the therein-reported magnetic specific heat. In addition, we present our estimate of the phonon background (green line). Vertical dashed lines are guide to the eye.

γ_c decreases, which coincides with the decrease of α_c in this temperature regime. This behavior corresponds to a regime of increased c_p, which signals the significance of in-plane ferromagnetic short-range correlations [11,26]. (3) At T_N what we observe is a negative cusp in γ_c that is associated with a jumplike decrease in α_c at the antiferromagnetic ordering transition. The fact that α_c decreases at T_N as well as in temperature regime (2) suggests that the antiferromagnetic interactions driving long-range order are relevant in regime (2), too.

TABLE II. Experimentally determined uniaxial pressure dependencies for $p \| c$ axis of several van der Waals materials. Materials exhibiting ferromagnetic order (at T_C) as well as ones with antiferromagnetic order (at T_N) are listed. We also show the result of our Grüneisen analysis in CrCl$_3$ at the crossover temperature T_C.

	AF/FM	T$_i$ [K]	$\frac{\partial T_i}{\partial p_c}$ $[\frac{\text{K}}{\text{GPa}}]$	$\frac{\partial \ln T_i}{\partial p_c}$ $[\frac{\%}{\text{GPa}}]$	Reference
CrCl$_3$	T_N	14	−20	−143	This work
CrCl$_3$	T_C	17	+7	+43	This work
Cr$_2$Ge$_2$Te$_6$	T_C	65	24.7	+38	[45]
CrI$_3$	T_C	61	1.7	+3	[44]
α-RuCl$_3$	T_{N3}	7	−10–14	−140–200	[46]

Qualitatively, as mentioned above, the sign of the anomaly at T_N implies $\partial\epsilon_2/\partial p_c < 0$, and it is straightforward to identify ϵ_2 with T_N. According to the Ehrenfest relation, uniaxial pressure dependence can be obtained from the experimental data by means of the anomalies $\Delta\alpha_c$ and Δc_p in the thermal expansion coefficient and in the specific heat, respectively, at T_N, using

$$\left.\frac{\partial T_N}{\partial p_c}\right|_B = T_N V_m \frac{\Delta\alpha_c}{\Delta c_p}. \tag{1}$$

By using $\Delta\alpha_c = -6.1 \times 10^{-6}\,\text{K}^{-1}$, $\Delta c_p = 0.9\,\text{J/(mol K)}$, and the molar volume [42] $V_m = 2.147 \times 10^{-4}\,\text{m}^3/\text{mol}$, applying Eq. (1) yields $\partial T_N/\partial p_c = -20\,\text{K/GPa}$. This corresponds to a relative pressure effect $\partial \ln T_N/\partial p_c$ of -143%/GPa. Hence, in contrast to isostructural materials evolving FM order, uniaxial strain applied perpendicular to the layers considerably suppresses long-range magnetic order in CrCl$_3$. The sign of pressure effect, however, agrees to the effects in α-RuCl$_3$ (see Table II) [43–47].

Summarizing the results of the Grüneisen and Ehrenfest analyses, uniaxial pressure along the c axis strongly suppresses long-range AFM order while it enhances ferromagnetic correlations. In an attempt to quantify the latter effect, we employ $\gamma_c(T = T_C) = 2 \times 10^{-6}\,\text{mol/J}$ [Fig. 10(c)]. By means of the Grüneisen relation, this yields the uniaxial pressure dependence $\partial\epsilon/\partial p_c \approx +7\,\text{K/GPa}$ at T_C. While there may be several, i.e., AFM (ϵ_2) and FM (ϵ_1), competing energy scales relevant at T_C, this result confirms the relevance of ferromagnetic interactions in this temperature regime as well as their enhancement upon application of $p \| c$ axis. In particular, we find competing effects of uniaxial pressure similar to what is observed in the hydrostatic experiments discussed above.

G. Pressure-dependent properties from first-principles theory

We have considered two types of interlayer magnetic stacking in our DFT calculations: FM and AFM configurations, as both were experimentally observed at ambient pressure in Cr$_{0.95}$Fe$_{0.05}$Cl$_3$. Initial calculations were carried out for pure CrCl$_3$. In the FM configuration, the system remains insulating under pressure, with the band gap decreasing modestly by ~0.1 eV between 0 and 5 GPa. A similar trend is observed for the AFM configuration, where the band gap reduces by ~0.2 eV over the same range. The Cr magnetic moment remains nearly constant at ~3 μ_B, consistent with the insulating nature of the system and the one-electron picture within DFT. Although many-body interactions and spin-orbit coupling could further influence the magnetic moment, they

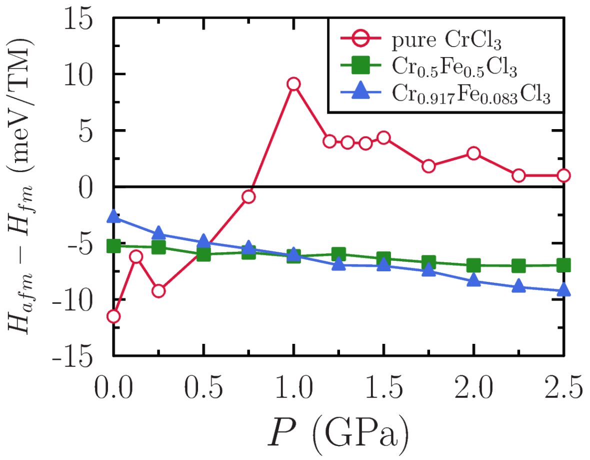

FIG. 11. Crystal structure of AFM-ordered undoped $CrCl_3$ in the hexagonal setting, pressure dependence of the enthalpy difference (ΔH) between the AFM and FM phases of Pure $CrCl_3$, $Cr_{0.917}Fe_{0.083}Cl_3$, and $Cr_{0.5}Fe_{0.5}Cl_3$, Pure $CrCl_3$ indicating an AFM-FM transition at around 1 GPa.

are not expected to significantly affect the AFM–FM energetic competition discussed here.

The structural optimization was performed using total energy minimization, where the lattice parameters and internal atomic positions were relaxed until Hellmann–Feynman forces were below 5 meV/Å and the stress tensor matched the applied external pressure within 0.1 GPa. The enthalpy difference $\Delta H = H_{\mathrm{AFM}} - H_{\mathrm{FM}}$, shown in Fig. 11, was used to evaluate the magnetic ground state under varying pressure. A negative ΔH corresponds to a stable AFM state, while a positive value indicates a preferred FM configuration. For pure $CrCl_3$, a pressure-induced transition from AFM to FM stacking is predicted at around 1 GPa. This DFT result is in excellent agreement with our experimental findings for $Cr_{0.95}Fe_{0.05}Cl_3$, which also exhibit a coexistence and competition between AFM and FM interlayer order at ambient pressure. With increasing pressure, the FM interaction becomes more dominant and AFM coupling is gradually suppressed, highlighting the pressure-driven magnetic crossover. To study the effect of Fe doping, we modeled two compositions, $Cr_{0.917}Fe_{0.083}Cl_3$ (8.3%) and $Cr_{0.5}Fe_{0.5}Cl_3$ (50%), by substituting Cr atoms with Fe in a checkerboard pattern within a supercell. For these doped systems, the enthalpy differences between AFM and FM configurations were evaluated as a function of pressure. Unlike the pure $CrCl_3$ case, the doped compositions do not exhibit a transition to FM order. In $Cr_{0.917}Fe_{0.083}Cl_3$, the AFM configuration becomes increasingly favorable with pressure, and in $Cr_{0.5}Fe_{0.5}Cl_3$, the AFM phase remains strongly stabilized throughout the pressure range of 0–3 GPa.

Notably, although 8.3% Fe is the lowest doping level we could simulate due to computational constraints, the result provides valuable insight into the behavior of $Cr_{0.95}Fe_{0.05}Cl_3$. The experimental composition exhibits a clear AFM–FM competition at ambient pressure and a pressure-enhanced stabilization of FM order. This is consistent with the trend observed in pure $CrCl_3$ DFT results, where FM order emerges beyond 1 GPa. However, our DFT simulations for $Cr_{0.917}Fe_{0.083}Cl_3$ indicate that even a small amount of Fe doping reinforces AFM stability, suppressing the FM state entirely within the accessible pressure range. These findings suggest that Fe doping counteracts the pressure-driven FM transition observed in the pure compound, reinforcing the robustness of AFM coupling in the doped systems.

Figure 12 shows the phase diagram of $Cr_{0.95}Fe_{0.05}Cl_3$; the experimental results reveal a complex magnetic structure characterized by the coexistence of AFM and FM interactions. Figure 12(a) presents the pressure dependence of the T_{N} and T_{C} for $Cr_{0.95}Fe_{0.05}Cl_3$ under an applied magnetic field of 0.001 T. With increasing pressure, both AFM and FM transition temperatures shift to lower values. Notably, the AFM transition is completely suppressed at approximately 2 GPa. The FM transition exhibits a narrow temperature width ($\sim$1 K) below 0.5 GPa, which broadens progressively with increasing pressure. Figure 12(b) shows the magnetic field dependence of T_{N} and T_{C} at ambient pressure. As the magnetic field increases, T_{N} shifts to lower temperatures and is fully suppressed above 0.4 T. In contrast, T_{C} increases with field strength, reaching 22 K at an applied field of 1 T. Figure 12(c) illustrates the magnetic field dependence of T_{N} and T_{C} under a pressure of 1.2 GPa. Both transition temperatures are reduced compared to the ambient-pressure case. However, with increasing fields, T_{C} rises from 6.8 to 10 K under an applied field of 0.4 T, while T_{N} decreases from 4.6 to 2 K under a field of 0.2 T. These observations indicate that the interlayer AFM interaction is suppressed, while the intralayer FM behavior is enhanced with the application of a pressure and magnetic field. These experimental findings are consistent with our DFT calculations on pure $CrCl_3$ compound, which suggests that applied pressure enhances virtual electron hopping between neighboring Cr ions via Cl ligands, thereby promoting ferromagnetic superexchange interactions [21].

IV. CONCLUSION

In summary, we have investigated the effects of both chemical doping and externally applied pressure on the 2D magnetic material $CrCl_3$. Chemical pressure was studied through Fe doping using XRD and Raman spectroscopy. XRD analysis confirmed that all synthesized samples are in a single phase, with no detectable impurity peaks. Fe doping leads to an increase in unit-cell volume with increasing Fe concentration, accompanied by an elongation of Cr–Cr and Cr–Cl bond distances. Raman spectroscopy revealed six Raman-active modes, and a redshift in these modes with increasing Fe content further confirms the unit-cell expansion due to chemical substitution. Externally applied pressure on $Cr_{0.95}Fe_{0.05}Cl_3$ induced notable changes in structural, vibrational, optical, and magnetic properties, especially around 9.2 GPa. Raman measurements showed a smooth blueshift of all six Raman-active modes up to 9.2 GPa. Above this pressure, the A_g^3 mode either disappeared or merged with the A_g^2 mode, likely due to modifications in bond lengths and angles. HP PL studies revealed an increase in the optical band gap up to 9.2 GPa, followed by a slight decrease up to 14.2 GPa. This trend, observed in both Raman and PL data, indicates the presence of IST in $Cr_{0.95}Fe_{0.05}Cl_3$ under HP.

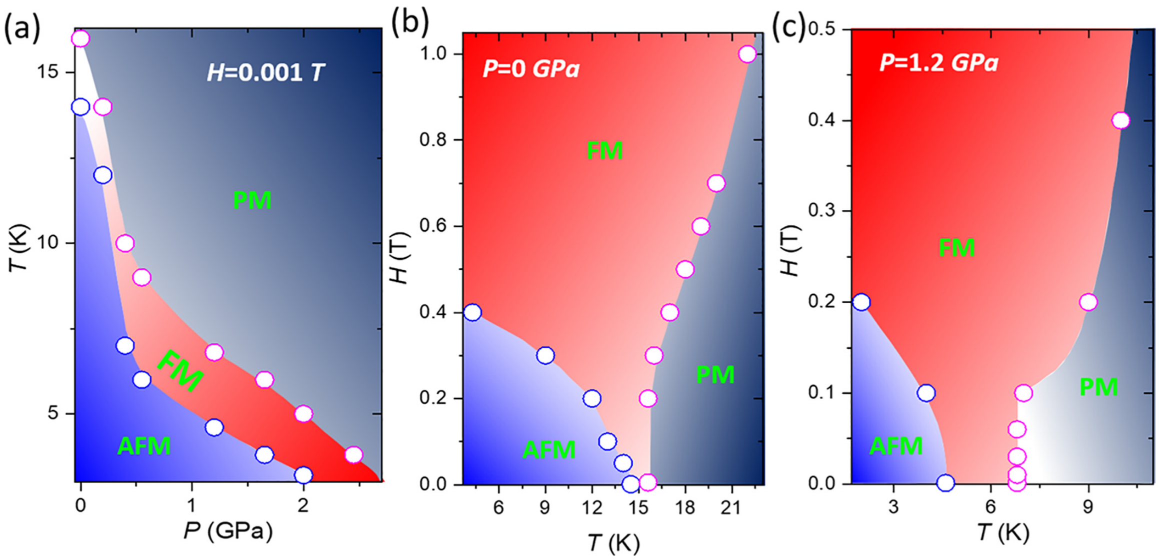

FIG. 12. Variation of T_N (blue open circle) and T_C (pink open circle) as a function of (a) applied pressure, (b) magnetic field at 0 GPa, and (c) magnetic field at 1.2 GPa for $Cr_{0.95}Fe_{0.05}Cl_3$.

Magnetization measurements under pressure confirmed the competition between AFM and FM orderings. AFM ordering is completely suppressed above 2 GPa, while the FM transition is enhanced above 0.5 GPa. At ambient pressure, magnetization under various magnetic field data reveals the coexistence of AFM and FM components; the AFM signal decreases with increasing field, while the FM component becomes dominant under higher fields. Thermal expansion measurements provided direct evidence of strong magnetoelastic coupling, with clear anomalies at the T_N and field-dependent contributions at elevated temperatures. In particular, Grüneisen analysis confirms the presence of competing, i.e., ferro- and antiferromagnetic interactions, the dependencies of which on uniaxial pressure along the c axis have been determined to be -143%/GPa and +43%/GPa, respectively. Our experimental observations are in good agreement with DFT calculations. DFT results predict pressure-enhanced FM superexchange interactions, and an AFM-to-FM interlayer stacking transition near 1 GPa is possible in pure $CrCl_3$. Furthermore, increasing Fe doping concentration was found to enhance AFM character at ambient pressure. Magnetization data at 1.2 GPa under varying magnetic fields confirmed exclusive FM ordering, with no AFM signal above 0.2 T, further supporting the theoretical predictions on pure $CrCl_3$. These findings underscore the potential of Fe-doped $CrCl_3$ for pressure-tunable magnetic and optoelectronic applications. The sensitive balance between FM and AFM states under external stimuli offers promising prospects for magnetic sensing devices. Future investigations into magnetoresistance and pressure-induced magnetism in Fe-doped $CrCl_3$ could further advance our understanding of this system, though such studies are beyond the scope of the present work.

ACKNOWLEDGMENTS

A.A. and M.-H. acknowledge support from the Advanced Materials Research Lab at the University of Sharjah. G.L., M.E.H., and M.H. acknowledge support from QRDI Project No. ARG01-0516-230179 at the University of Doha for Science and Technology, Qatar, and A.A. acknowledges support from the same project at HBKU, Qatar. Support by Deutsche Forschungsgemeinschaft (DFG) under Germany's Excellence Strategy EXC2181/1-390900948. (The Heidelberg STRUCTURES Excellence Cluster) is gratefully acknowledged. L.G. acknowledges funding by the International Max-Planck Research School for Quantum Dynamics (IMPRS-QD) Heidelberg. The Swedish Research Council (Vetenskapsrådet, VR) Grant No. 2016–05980, Grant No. 2019–05304, and Grant No. 2024–04986, and Knut and Alice Wallenberg Foundation Grants No. 2018.0060, No. 2021.0246, and No. 2022.0108 are acknowledged. The Wallenberg Initiative Materials Science for Sustainability (WISE) funded by the Knut and Alice Wallenberg Foundation is also acknowledged. The computations/data handling were enabled by resources provided by the National Academic Infrastructure for Supercomputing in Sweden (NAISS), partially funded by the Swedish Research Council through Grant Agreement No. 2022–06725. O.E. also acknowledges support from STandUPP and eSSENCE, as well as the ERC (FASTCORR-Synergy Grant No. 854843). V.B. acknowledges support by the Swedish Research Council through Grant No. 2024-05206.

DATA AVAILABILITY

The data that support the findings of this article are not publicly available. The data are available from the authors upon reasonable request.

---

[1] K. S. Novoselov, A. K. Geim, S. V. Morozov, D. E. Jiang, Y. Zhang, S. V. Dubonos, I. V. Grigorieva, and A. A. Firsov, Electric field effect in atomically thin carbon films, Science **306**, 666 (2004).

[2] A. P. Balan, A. B. Puthirath, S. Roy, G. Costin, E. F. Oliveira, M. A. Saadi, V. Sreepal, R. Friedrich, P. Serles, A. Biswas, and S. A. Iyengar, Non-van der Waals quasi-2D materials; Recent advances in synthesis, emergent properties and applications, Mater. Today **58**, 164 (2022).

[3] C. Li, Q. Cao, F. Wang, Y. Xiao, Y. Li, J. J. Delaunay, and H. Zhu, Engineering graphene and TMDs based van der Waals heterostructures for photovoltaic and photoelectrochemical solar energy conversion, Chem. Soc. Rev. **47**, 4981 (2018).

[4] H. Xu, Y. Xue, Z. Liu, Q. Tang, T. Wang, X. Gao, Y. Qi, Y. P. Chen, C. Ma, and Y. Jiang, Van der Waals heterostructures for photoelectric, memory, and neural network applications, Small Sci. **4**, 2300213 (2024).

[5] M. A. McGuire, Cleavable magnetic materials from van der Waals layered transition metal halides and chalcogenides, J. Appl. Phys. **128**, 110901 (2020).

[6] E. Elahi, G. Dastgeer, G. Nazir, S. Nisar, M. Bashir, H. A. Qureshi, D. K. Kim, J. Aziz, M. Aslam, K. Hussain, and M. A. Assiri, A review on two-dimensional (2D) magnetic materials and their potential applications in spintronics and spin-caloritronic, Comput. Mater. Sci. **213**, 111670 (2022).

[7] L. Thiel, Z. Wang, M. A. Tschudin, D. Rohner, I. Gutiérrez-Lezama, N. Ubrig, M. Gibertini, E. Giannini, A. F. Morpurgo, and P. Maletinsky, Probing magnetism in 2D materials at the nanoscale with single-spin microscopy, Science **364**, 973 (2019).

[8] K. Basak, M. Ghosh, S. Chowdhury, and D. Jana, Theoretical studies on electronic, magnetic and optical properties of two dimensional transition metal trihalides, J. Phys. Condens. Matter **35**, 233001 (2023).

[9] J. L. Lado and J. Fernández-Rossier, On the origin of magnetic anisotropy in two dimensional CrI_3, 2D Mater. **4**, 035002 (2017).

[10] A. S. Ahmad, Y. Liang, M. Dong, X. Zhou, L. Fang, Y. Xia, J. Dai, X. Yan, X. Yu, J Dai, and G. J. Zhang, Pressure-driven switching of magnetism in layered $CrCl_3$, Nanoscale **12**, 22935 (2020).

[11] M. A. McGuire, G. Clark, S. KC, W. M. Chance, G. E. Jellison, Jr., V. R. Cooper, X. Xu, and B. C. Sales, Magnetic behavior and spin-lattice coupling in cleavable van der Waals layered $CrCl_3$ crystals, Phys. Rev. Mater. **1**, 014001 (2017).

[12] Z. Zhang, J. Shang, C. Jiang, A. Rasmita, W. Gao, and T. Yu, Direct photoluminescence probing of ferromagnetism in monolayer two-dimensional $CrBr_3$, Nano Lett. **19**, 3138 (2019).

[13] I. Tsubokawa, On the magnetic properties of a $CrBr_3$ single crystal, J. Phys. Soc. Jpn. **15**, 1664 (1960).

[14] M. A. McGuire, H. Dixit, V. R. Cooper, and B. C. Sales, Coupling of crystal structure and magnetism in the layered, ferromagnetic insulator CrI_3, Chem. Mater. **27**, 612 (2015).

[15] Y. Liu, L. Wu, X. Tong, J. Li, J. Tao, Y. Zhu, and C. Petrovic, Thickness-dependent magnetic order in CrI_3 single crystals, Sci. Rep. **9**, 13599 (2019).

[16] P. W. Anderson, Antiferromagnetism. Theory of superexchange interaction, Phys. Rev. **79**, 350 (1950).

[17] J. B. Goodenough, Theory of the role of covalence in the perovskite-type manganites [La, M(II)]MnO_3, Phys. Rev. **100**, 564 (1955).

[18] J. Kanamori, Superexchange interaction and symmetry properties of electron orbitals, J. Phys. Chem. Solids **10**, 87 (1959).

[19] B. Sadhukhan, A. Bergman, Y. O. Kvashnin, J. Hellsvik, and A. Delin, Spin-lattice couplings in two-dimensional CrI_3 from first-principles computations, Phys. Rev. B **105**, 104418 (2022).

[20] L. Zhang, Y. Tang, A. R. Khan, M. M. Hasan, P. Wang, H. Yan, T. Yildirim, J. F. Torres, G. P. Neupane, Y. Zhang, and Q. Li, 2D materials and heterostructures at extreme pressure, Adv. Sci. **7**, 2002697 (2020).

[21] S. Mondal, M. Kannan, M. Das, L. Govindaraj, R. Singha, B. Satpati, S. Arumugam, and P. Mandal, Effect of hydrostatic pressure on ferromagnetism in two-dimensional CrI_3, Phys. Rev. B **99**, 180407(R) (2019).

[22] A. Ghosh, D. Singh, T. Aramaki, Q. Mu, V. Borisov, Y. Kvashnin, G. Haider, M. Jonak, D. Chareev, S. A. Medvedev, R. Klingeler, M. Mito, E. H. Abdul-Hafidh, J. Vejpravova, M. Kalbac, R. Ahuja, O. Eriksson, and M. Abdel-Hafiez, Exotic magnetic and electronic properties of layered CrI_3 single crystals under high pressure, Phys. Rev. B **105**, L081104 (2022).

[23] A. O. Fumega, S. Blanco-Canosa, H. Babu-Vasili, P. Gargiani, H. Li, J. S. Zhou, F. Rivadulla, and V. Pardo, Electronic structure and magnetic exchange interactions of Cr-based van der Waals ferromagnets. A comparative study between $CrBr_3$ and $Cr_2Ge_2Te_6$, J. Mater. Chem. C **8**, 13582 (2020).

[24] M. Hong, L. Dai, H. Hu, X. Zhang, C. Li, and Y. He, Pressure-driven structural phase transitions and metallization in the two-dimensional ferromagnetic semiconductor $CrBr_3$, Dalton Trans. **52**, 7290 (2023).

[25] O. Lis, D. Kozlenko, S. Kichanov, E. Lukin, I. Zel, and B. Savenko, Structural, magnetic and vibrational properties of van der Waals ferromagnet $CrBr_3$ at high pressure, Materials **16**, 454 (2023).

[26] S. Mondal, A. Midya, M. M. Patidar, V. Ganesan, and P. Mandal, Magnetic and magnetocaloric properties of layered van der Waals $CrCl_3$, Appl. Phys. Lett. **117**, 092405 (2020).

[27] M. Hong, L. Dai, H. Hu, X. Zhang, C. Li, and Y. He, Pressure-induced structural phase transition and metallization of $CrCl_3$ under different hydrostatic environments up to 50.0 GPa, Inorg. Chem. **61**, 4852 (2022).

[28] H. Wang, F. Fan, S. Zhu, and H. Wu, Doping enhanced ferromagnetism and induced half-metallicity in CrI_3 monolayer, Eur. Phys. Lett **114**, 47001 (2016).

[29] S. Pan, Y. Bai, J. Tang, P. Wang, Y. You, G. Xu, and F. Xu, Growth of high-quality CrI_3 single crystals and engineering of its magnetic properties via V and Mn doping, J. Alloys Compd. **908**, 164573 (2022).

[30] F. Wang, Y. Zhang, W. Yang, J. Zhang, H. Zhang, and X. Xu, Topological half-metallic features in alkali metal doped $CrCl_3$ monolayers, Phys. Rev. B **107**, 174405 (2023).

[31] A. Ebrahimian, A. Dyrdał, and A. Qaiumzadeh, Control of magnetic states and spin interactions in bilayer $CrCl_3$ with strain and electric fields: An *ab initio* study, Sci. Rep. **13**, 5336 (2023).

[32] D. A. Chareev, M. E. Khan, D. Karmakar, A. N. Nekrasov, M. S. Nickolsky, O. Eriksson, A. Delin, A. N. Vasiliev, and M. Abdel-Hafiez, Correction to stable sulfuric vapor transport and liquid-sulfur growth on transition metal dichalcogenides, Cryst. Growth Des. **23**, 4720 (2023).

[33] R. Küchler, T. Bauer, M. Brando, and F. Steglich, A compact and miniaturized high resolution capacitance dilatometer for measuring thermal expansion and magnetostriction, Rev. Sci. Instrum. **83**, 095102 (2012).

[34] R. Küchler, A. Wörl, P. Gegenwart, M. Berben, B. Bryant, and S. Wiedmann, The world's smallest capacitive dilatometer, for high-resolution thermal expansion and magnetostriction in high magnetic fields, Rev. Sci. Instrum. **88**, 083903 (2017).

[35] J. Werner, W. Hergett, M. Gertig, J. Park, C. Koo, and R. Klingeler, Anisotropy-governed competition of magnetic phases in the honeycomb quantum magnet $Na_3Ni_2SbO_6$ studied by dilatometry and high-frequency ESR, Phys. Rev. B **95**, 214414 (2017).

[36] G. Kresse and J. Furthmüller, Efficient iterative schemes for ab initio total-energy calculations using a plane-wave basis set, Phys. Rev. B **54**, 11169 (1996).

[37] See Supplemental Material at http://link.aps.org/supplemental/10.1103/v7l7-f3wj for EDX analysis confirming Fe substitution and additional temperature-dependent magnetization data under various pressures and applied fields.

[38] C. N. Avram, A. S. Gruia, M. G. Brik, and A. M. Barb, Calculations of the electronic levels, spin-Hamiltonian parameters and vibrational spectra for the $CrCl_3$ layered crystals, Physica B **478**, 31 (2015).

[39] I. Kanesaka, H. Kawahara, A. Yamazaki, and K. Kawai, The vibrational spectrum of MCl_3 ($M = Al$, Cr and Fe), J. Mol. Struct. **146**, 41 (1986).

[40] R. Klingeler, J. Geck, S. Arumugam, N. Tristan, P. Reutler, B. Büchner, L. Pinsard-Gaudart, and A. Revcolevschi, Pressure-induced melting of the orbital polaron lattice in $La_{1-x}Sr_xMnO_3$, Phys. Rev. B **73**, 214432 (2006).

[41] P. Gegenwart, Grüneisen parameter studies on heavy fermion quantum criticality, Rep. Prog. Phys. **79**, 114502 (2016).

[42] W. N. Hansen and M. Griffel, Heat capacities of CrF_3 and $CrCl_3$ from 15 to 300 K, J. Chem. Phys. **28**, 902 (1958).

[43] M. Roslova, J. Hunger, G. Bastien, D. Pohl, H. M. Haghighi, A. U. Wolter, A. Isaeva, U. Schwarz, B. Rellinghaus, K. Nielsch, and B. Büchner, Detuning the honeycomb of the α-$RuCl_3$ Kitaev lattice: A case of Cr^{3+} dopant, Inorg. Chem. **58**, 6659 (2019).

[44] J. Arneth, M. Jonak, S. Spachmann, M. Abdel-Hafiez, Y. O. Kvashnin, and R. Klingeler, Uniaxial pressure effects in the two-dimensional van der Waals ferromagnet CrI_3, Phys. Rev. B **105**, L060404 (2022).

[45] S. Spachmann, A. Elghandour, S. Selter, B. Büchner, Aswartham S, and R. Klingeler, Strong effects of uniaxial pressure and short-range correlations in $Cr_2Ge_2Te_6$, Phys. Rev. Res. **4**, L022040 (2022).

[46] M. He, X. Wang, L. Wang, F. Hardy, T. Wolf, P. Adelmann, T. Brückel, Y. Su, and C. Meingast, Uniaxial and hydrostatic pressure effects in α-$RuCl_3$ single crystals via thermal-expansion measurements, J. Phys.: Condens. Matter **30**, 385702 (2018).

[47] S. Spachmann, S. Selter, B. Büchner, S. Aswartham, and R. Klingeler, Strong uniaxial pressure dependencies evidencing spin-lattice coupling and spin fluctuations in $Cr_2Ge_2Te_6$, Phys. Rev. B **107**, 184421 (2023).